Effect of Mn^{2+} Replacement on the Optical, Structural, and Magnetic Properties of Copper Ferrite Nanoparticles

Nasser K. Hejazy

Department of Technology and Applied Science, Al-Quds Open University, Faculty of Science, Gaza GFM3+FPW, Gaza Strip, Palestine

ABSTRACT: Co-precipitation was employed to successfully synthesise nanoparticles of copper ferrite $Cu_{1-x}Mn_xFe_2O_4$ (x= 0.2, 0.4, 0.6, 0.8, and 1.0) that were both undoped and cobalt-doped. X-ray diffraction (XRD) demonstrated that all samples exhibited a single cubic spinel structure with clear outlines. The XRD measurements showed an increase in crystallite size from 10.2 to 20 nm. As the Mn^{2+} content increased, the lattice parameter rose from 8.332 to 8.371. With a higher concentration of Mn^{2+} ions, it was observed that the band gap energy of nanoferrites decreased from 3.65 to 3.20 eV. In copper ferrite matrices, it was found that the Mn^{2+} ratio increased along with the luminescence intensity. The graph indicates that saturation magnetisation increased with rising manganese ion concentration. According to the M-H loops, saturation magnetisation spiked as the manganese ion concentration increased.

KEYWORDS: Band gap; Cu-Mn Ferrites; Magnetism; Nanoparticles; Optical properties; XRD

1. INTRODUCTION

Spinel-structured magnetic nanoparticles of transition metal ferrites are of significant interest for biological, environmental, and industrial applications. They are considered alternatives for many applications due to their exceptional properties, including high saturation magnetisation, high coercivity, great chemical stability, and mechanical toughness [1]. Recent advances in materials science, particularly in the health sciences, have been focused on superparamagnetic iron oxide nanoparticles (SPIONs) and their dispersions. [2]. The SPIONs that have high saturation magnetisation are seen as promising for the biomedical industry due to their intriguing properties [3,4].

Spinel ferrite nanoparticles MFe_2O_4 have extensive applications including contrast enhancement in magnetic storage systems, photomagnetic materials, and magnetic resonance imaging (MRI) [5-8].

The structure of the ferrites is based on the size, and distribution of the metal ions inside the tetrahedral, octahedral positions of the spinel structure, and the chemical identity of the divalent metal (MII) [9, 10]. The general formula for spinel ferrites is MFe_2O_4, in which M is an ion of a divalent metal, and Fe is located in the +3 oxidation state. [11–14]. Spinel ferrites were discovered in two forms, normal and inverse, where the inverse represents the majority [15,16]. The ions M^{2+} are present in the occupied tetrahedral positions in a typical spinel, whereas the ions Fe^{3+} are present in the octahedral positions [17,18]. However, the occupied octahedral sites contain all of the M^{2+} ions and 50% of the Fe^{3+} ions, with the remaining 25% of the Fe^{3+} ions occupying the inverse spinel's tetrahedral sites.

MnFe$_2$O$_4$, or manganese ferrite, is a type of soft magnetic material that has distinct properties such as high magnetic permeability, saturation magnetisation (Ms), Curie temperature, and low losses. Recent applications of MnFe$_2$O$_4$ include the production of radio frequency coils, transformer cores, rod antennas, sensors, catalysts, microwave structures, computer memory chips, magnetic storage media, and electronic engineering [19–21].

CuFe$_2$O$_4$ along with Cu^{2+} ions forms an inverse spinel structure with distorted octahedral positions. Additionally, Fe^{3+} ions are scattered in tetrahedral and octahedral positions, differing from Mn^{2+} ions in terms of magnetic moment and ionic radius [22,23]. Depending on the amount of the precursor solutions, the addition of Mn to CuFe$_2$O$_4$ can lead to deformed spinel formations. Mn-Cu Ferrite (Mn$_x$Cu$_{1-x}$Fe$_2$O$_4$) is among the top combined light ferrites because of its high resistivity, immoderate saturation magnetisation, excessive permeability, controllable length and structural features, as well as its convenient synthesis method and tuneable electromagnetic properties [24, 25]. Transformer cores [26], noise filters, antennas, microwave instruments [27], multilayer chip capacitors, persistent magnets [28], yoke coils, and high permeability devices [29] are just a few of the many uses for Mn-Cu ferrite. Mixed manganese-copper nanoferrites have been prepared using a variety of techniques [30–36].

Sol-gel assisted by microwaves [33,34], co-precipitation [31,34], sol-gel [37,38], ceramic [35], microemulsion [39], and soft chemistry approaches [36] are a few examples of these techniques. Among all of these methods, co-precipitation has become the preferred one. In order to achieve this, additional metallic salts in the suspension must also precipitate at the same time, an agent for precipitation (or ligand) must be used, and the precipitate must then be heated to cause it to decompose [35].

In comparison to other procedures, it has numerous benefits, including adequate stoichiometry manipulation, low running temperature, low costs, and better dispersion of the constituents in the resultant ferrites [27,40]. Researchers are focusing on the impact of the replacement with other cations to enhance the material characteristics of copper spinel ferrites. [41].

The copper ferrite characteristics have been shown to vary to accommodate different metal cation replacements [42–44]. Investigations into Mn replacement in various ferrite systems have revealed its major influence on the structural, electrical, and magnetic characteristics. $MnFe_2O_4$ and $CuFe_2O_4$ have both been the subject of much research, however, no studies on mixed cc ferrites have been published. Rath et al. [45] have pointed out the dependence of Mn-Zn ferrite on cation distribution of particle size, lattice parameter, and magnetic characteristics. The anomalism of copper manganese ferrites $Cu_{1-x}Mn_xFe_2O_4$ (0 x 0.7) was examined by Azab et al.[46]. Salah et al. produced copper-doped $MnFe_2O_4$ using co-precipitation to discover that when the amount of copper increases, the crystallite size and lattice parameter have an inverse relation with the inclining electrical conductivity [47].

Moreover, Vijaya et al. [48] synthesized $Cu_{1-x}Mn_xFe_2O_4$ using a microwave combustion technique supported by Urea. They claimed that the Lattice parameter had decreased from 8.477 to 8.455 because the Cu^{2+} dopant has a smaller ionic radius than Mn^{2+}, whereas, by using the auto-combustion technique, Jayaprakash et al. [49] examined how the temperature at which the annealing occurred affected the size, agnetic, and dielectric characteristics of copper ferrite nanoparticles replaced with manganese. They determined that the sizes of crystallite range between ~9-45 nm. In a previous study, the researchers showed [50] how zinc substitution affected the structural, morphological, optical, and magnetic characteristics of copper ferrite NPs assembled using co-precipitation.

Until now there has not been any thorough investigation into the luminous and magnetic characteristics of Mn^{2+} doped $CuFe_2O_4$ nanoferrites produced using the precipitation method. Using the precipitation approach, doped copper ferrite nanoparticles with the chemical formula $Cu_{1-x}Mn_xFe_2O_4$ (x= 0.2, 0.4, 0.6, 0.8, and 1.0) were produced in this study. Hence, it has been investigated how the substitution of manganese ions affects the structural, magnetic, and optical characteristics of copper ferrite nanoparticles.

2. MATERIALS AND METHODS

The precipitation method was used to create nanoferrites with the general formula $Cu_{1-x}Mn_xFe_2O_4$ ($0 \leq x \leq 1$) [50], and **Figure** 1 depicts the synthesis process for the creation of nanoparticles. Following that, 25 mL of deionised water was used to dissolve the preferred stoichiometric percentage amounts of high-purity copper sulphate pentahydrate ($CuSO_4.5H_2O$), ferrous ammonium sulphate hexahydrate (($NH_4)_2Fe(SO_4)_2.6H_2O$), and manganese sulphate monohydrate ($MnSO_4.H_2O$). The mixtures were aggressively and continuously magnetically stirred for 60 minutes. Moreover, after 20 mmol of oxalic acid had been dissolved in an equivalent amount of deionised water and agitated magnetically for an hour, metal salts were added dropwise to the mixture. The precipitates were then repeatedly washed before being dried at 373 K in an oven. With a mortar and pestle, the dry precipitates were ground into powder form of the nanostructure, $Cu_{1-x}Mn_xFe_2O_4$. The powdered material was finally sintered at 500°C for three hours in a muffle furnace as shown in **Figure** 1.
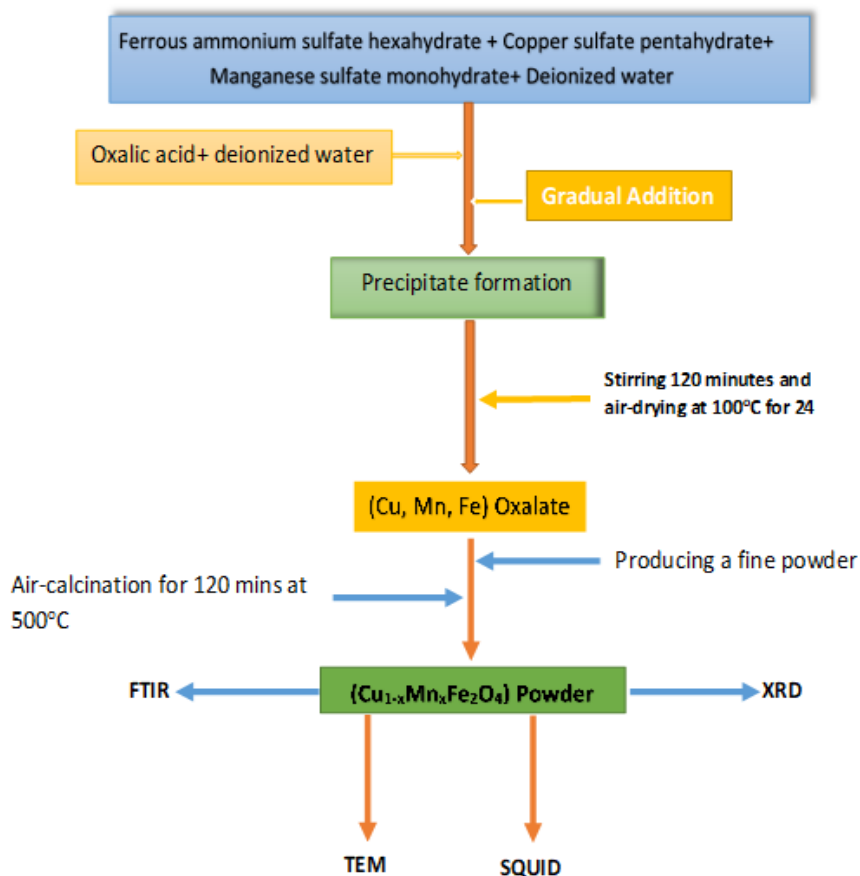
Figure 1: Process diagram of the experiment

2.1 Characterization

A powder X-ray diffractometer (XRD) was utilised to identify the crystal structure that was recorded at ambient temperature using the XDS 2000, CuKα radiation of wavelength equal to 1.5406, manufactured by Scintac Inc. in the USA for the purpose of confirming that the sample contains chemical bonding. The presence of chemical bonds in the sample was also determined using Fourier-transform infrared spectroscopy, utilising a Frontier (Perkin Elmer) spectrophotometer in the spectral range of 200-400 cm-1. Also, The band gap energy and optical absorption properties were determined using an HP 8453/UV-Vis absorption spectrometer.

Furthermore, luminescence experiments were conducted using a fluorescence spectrophotometer (Perkin-Elmer LS 50B), while the morphological analyses of created nanoparticles were examined with a Tecnai F300 transmission electron microscope (TEM). Finally, the researcher investigated the magnetism of produced nanoferrites using extensive field-dependent magnetisation metrics in domains up to 3,183.09 kA/m (40 kOe) using superconducting quantum interference device (SQUID) Quantum Design MPMS XL-7 magnetometer in RSO mode.

3.   RESULTS

3.1. Structural Analysis

The X-ray diffraction (XRD) investigation revealed the crystal arrangement and phase clarity of the specimens. $Cu_{1-x}Mn_xFe_2O_4$ XRD patterns in range 2θ between 20° and 70° are shown in **Figure** 2. Where x = 0.0, 0.2, 0.4, 0.6, 0.8, and 1.0.
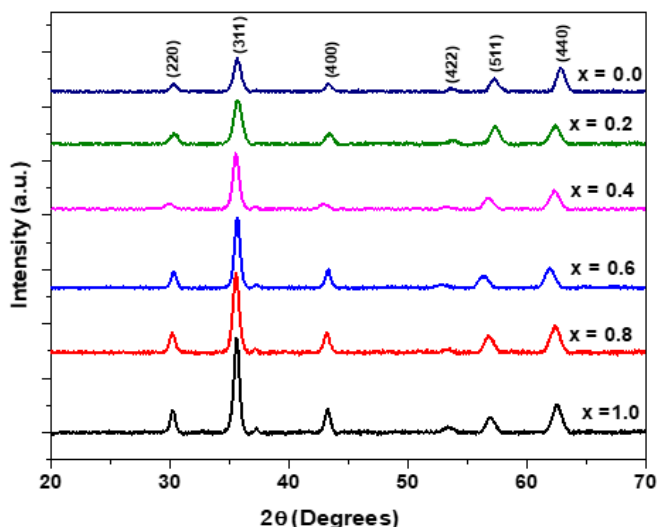
Figure 2: XRD analysis of Cu$_{1-x}$Mn$_x$Fe$_2$O$_4$ (x = 0.0, 0.2, 0.4, 0.6, 0.8 and 1.0) nanoferrites.

The reflections of crystal planes (220), (311), (400), (422), (511), and (440) are responsible for the peaks observed at 29.8º, 35.46º, 43.74º, 53.86º, 56.77º, and 62.35º, respectively. The detected diffraction peaks demonstrated the single-phase cubic spinel structure of these nanoparticles. The XRD results from this work and the CuFe$_2$O$_4$ nanoparticles XRD result are consistent [51]. All of the identified XRD peaks (e.g., Fe$_2$O$_3$, MnO, CuO, etc.) result from the cubic spinel lattice because no other impurity phases could be observed, demonstrating their single-phase origin.

$$a^2 = d^2\left(h^2 + k^2 + l^2\right) \qquad (1)$$

The aforementioned relations [52] were used to derive the lattice constants (a), which are then listed in **Table** 1.

$$a^2 = d^2\left(h^2 + k^2 + l^2\right) \qquad (1)$$

Table 1: Lattice constant and particle size of Cu$_{1-x}$Mn$_x$Fe$_2$O$_4$

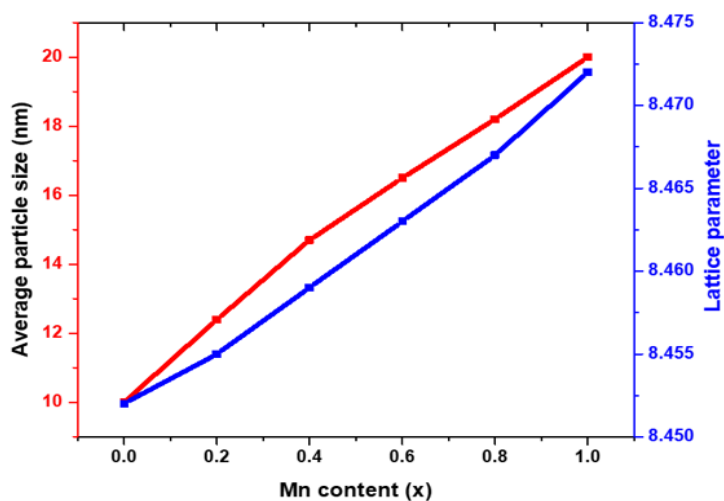| Composition	Lattice constant (Å)	Particle size (nm)
0.0	8.452	10.2
0.2	8.455	12.4
0.4	8.459	14.7
0.6	8.463	16.1
0.8	8.467	18.3
1.0	8.472	20

Figure 3. Variation in the average crystallite measurement and the lattice parameter with Mn content.

According to **Vegard's law** [53], it was found that the unit cell characteristics of the Mn^{2+} that replaced the Cu^{2+} ferrite increased proportionally with the level of Mn^{2+} ions in the mixture, as depicted in **Figure** 3.

Figure 3 illustrates the variance in lattice parameter values for ferrites containing Mn^{2+} and demonstrates that this is because Mn^{2+} has a smaller ionic radius (0.92 Å) than Cu^{2+} (0.73 Å), which causes the lattice parameter to increase as Mn^{2+} level increases [52]. The lattice parameter increased when the Cu^{2+} ion was substituted with Mn^{2+} in this study, which may be connected to changes in higher composition in many Fe^{3+} ions transferred to the B site from the A site [54]. The lattice constant was discovered to be between 8.452 and 8.473 Å. As a consequence, the lattice parameter values for each sample agreed with those reported in previous published papers [53]. Additionally, the average size of the crystallites in the specimens was calculated using **Scherrer's** equation. [55] as:

$$D = \frac{k\lambda}{(B\cos\theta)} \quad (2)$$

Where B is the line broadening at half the maximum intensity, D is the average crystallite size, K is roughly equal to 0.9, and λ is the X-ray wavelength.

The reduced average crystallite size was attributed to the peak's broadness, and **Table** 1's estimated particle sizes for the samples were determined to be between 10.2 and 20 nm. Furthermore, as the Mn^{2+} ion concentration in $CuFe_2O_4$ ferrite increases, so does the average particle size. **Figure** 3 shows the fluctuation in mean crystallite size with manganese content.

3.2 Transmission Electron Microscopy (TEM) Studies

The histograms and TEM morphology of the $Cu_{1-x}Mn_xFe_2O_4$ (x = 0.0, 0.2, 0.4, 0.6, 0.8 and 1.0) nanoferrite were used to determine the morphologies of the nickel doped copper ferrite nanoparticles. These results are presented in **Figures** 4 and 5. All Cu-Mn samples display sphere-shaped particles in agglomeration, as seen by the TEM images (Figures 4(a-f)). Pure $CuFe_2O_4$ nanoparticles are visible in **Figure** 4(a), and images of homogeneous and aggregated Cu-Mn nanoferrite are shown in **Figure** 4(b) to (f). The magnetic interactions between the particles caused the nanoparticles to aggregate [56].
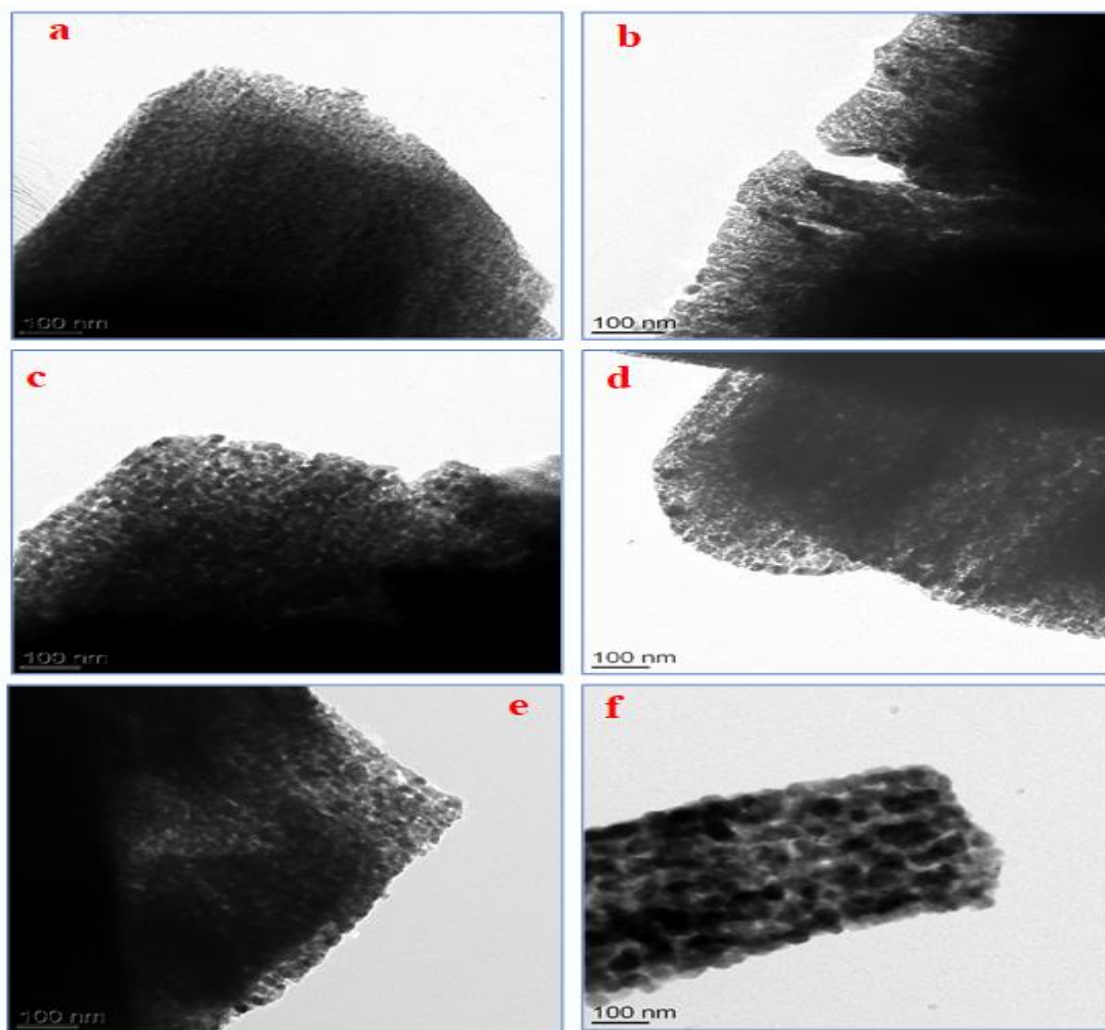
Figure 4 (a-f): TEM micrographs of Cu₁₋ₓMnₓFe₂O₄ (x = 0.0, 0.2, 0.4, 0.6, 0.8 and 1.0)

Figure 5(a-f) displayed histograms for specimens of Mn-doped $CuFe_2O_4$ with averaged particle sizes that varied between 10 to 27 nm. As a result, it was shown that the size of $Cu_{1-x}Mn_xFe_2O_4$ nanoparticles decreases as the level of copper increases. Also, the sizes agreed with the crystallite measurements found in the XRD data.
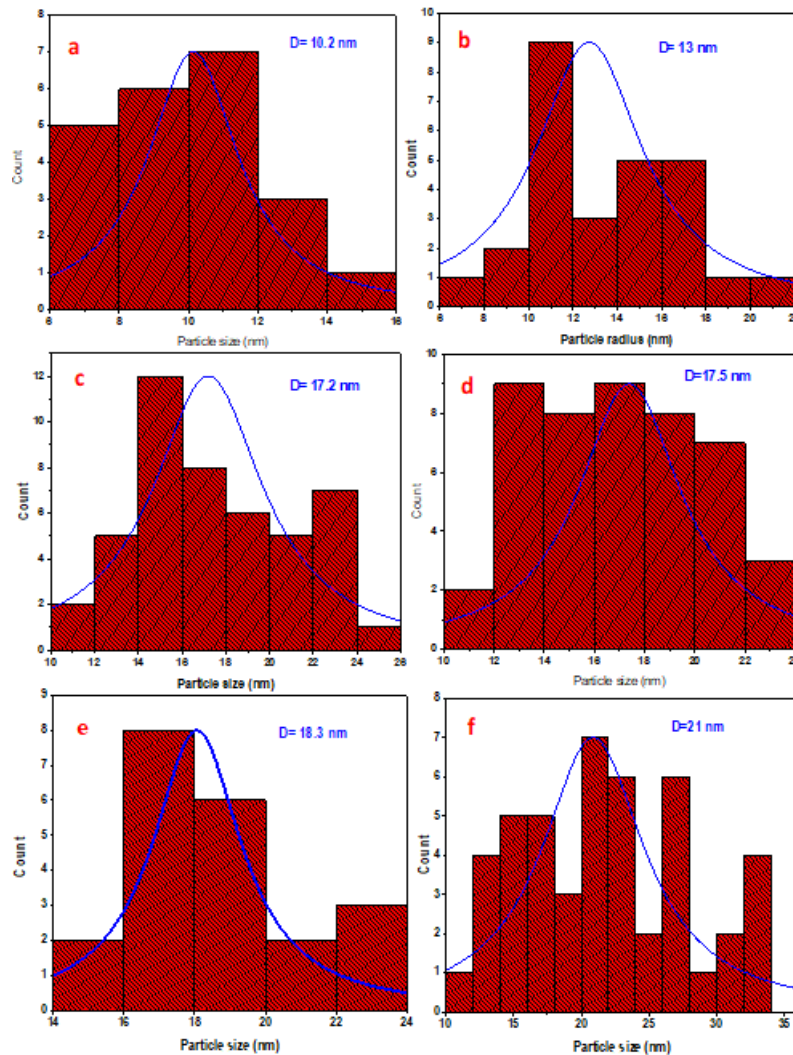

Figure 5 (a-f): Histograms of $Cu_{1-x}Mn_xFe_2O_4$ (x = 0.0, 0.2, 0.4, 0.6, 0.8 and 1.0)

3.3 Energy Dispersive X-ray Spectroscopy (EDX) Analysis

EDX spectroscopy is a known analytical tool for figuring out specimen contents. The EDX examination corroborated the chemical assessment of $Cu_{1-x}Mn_xFe_2O_4$ x = (0.0, 0.2, 0.6, 0.8, and 1.0) nanostructures, and the findings are displayed in **Figure** 6. (a-f). Iron (Fe), manganese (Mn), copper (Cu), and oxygen (O) were detected in the EDX spectrum, demonstrating the excellent clarity of the produced powders. Hence, there was excellent agreement between the EDX and XRD results.
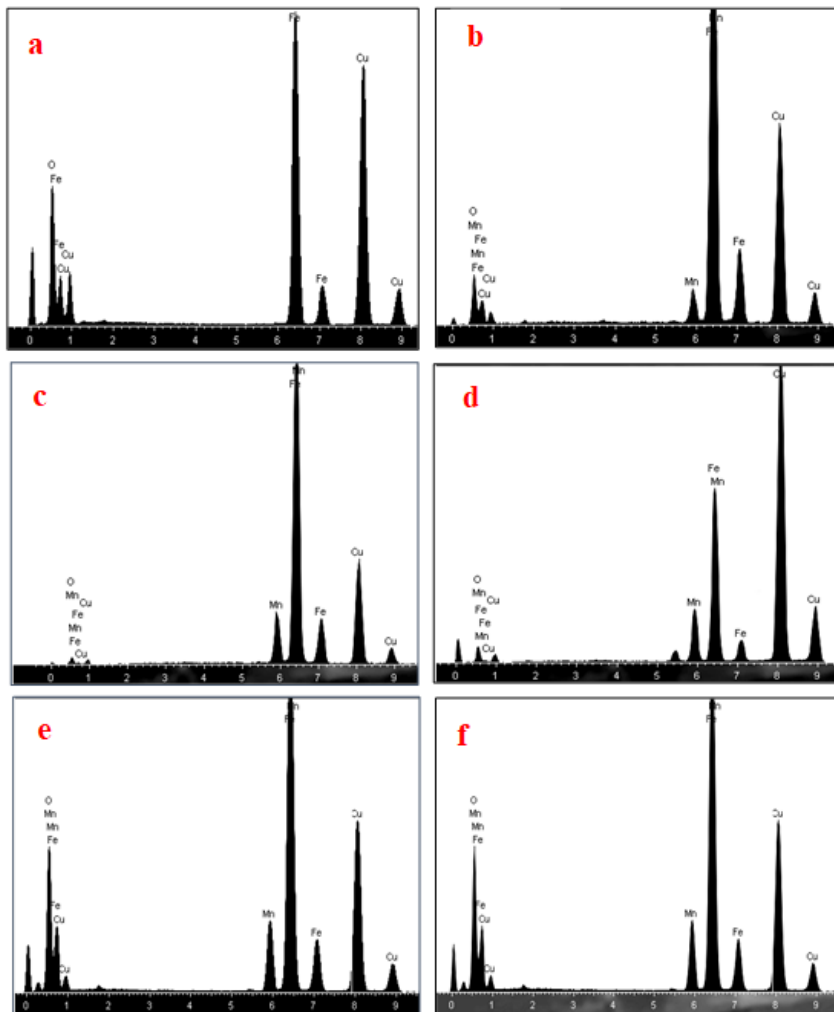
Figure 6 (a-f): EDX spectrum of Cu$_{1-x}$Mn$_x$Fe$_2$O$_4$ (x = 0.0, 0.2, 0.4, 0.6, 0.8 and 1.0)

3.4 Ultraviolet-visible (UV-Vis) Absorption Researches

Figure 7 displays the UV-Vis optical spectrums of Cu$_{1-x}$Mn$_x$Fe$_2$O$_4$ nanoferrites that were captured between 240 nm to 600 nm wavelength range. The anticipation of the linear component of **Tauc's** relation given [57], was employed to determine the optical band gap energy (E$_g$) for produced nanoferrites.

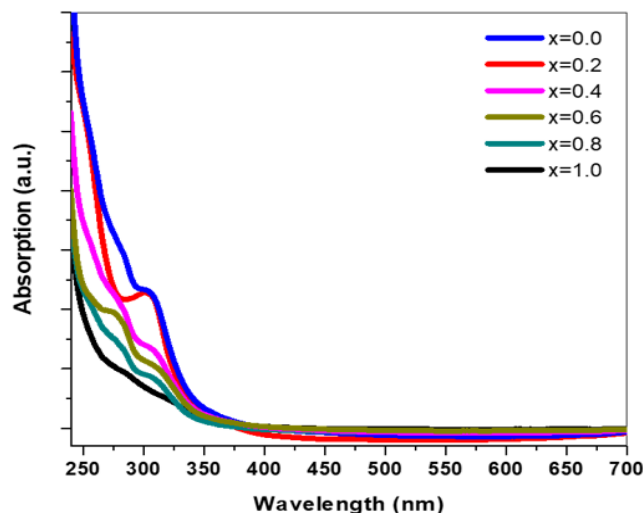$$(\alpha h\upsilon)^2 = A(h\nu - E_g) \qquad (2)$$

**Figure 7: UV-vis. spectra of Cu$_{1-x}$Mn$_x$Fe$_2$O$_4$
(x= 0.0, 0.2, 0.4, 0.6, 0.8 and 1) nanoferrites.**

The absorption coefficient, **Plank's constant**, light frequency, band gap, and proportionality consistency are represented respectively by the symbols α, h, v, E_g, and A.

The relationship between $(\alpha h v)^2$ and hv is displayed in **Figure** 8, and the point of intersection is taken into account as the band gap energy. $Cu_{1-}Mn_xFe_2O_4$ band gap energies were calculated and they showed 3.61, 3.56, 3.41, 3.31, and 3.23, respectively (**Figure** 8). **Figure** 8 demonstrates

unequivocally that the band gap of the Mn-doped $CuFe_2O_4$ samples is smaller than that of the pure $CuFe_2O_4$ samples. As cobalt concentration increases, the optical absorption spectrum shows extreme red shift in the band gap that results from the quantum size effects. Moreover, Joseph et al. [58] noted the same effect: the band gap values increased significantly as particle size increased.
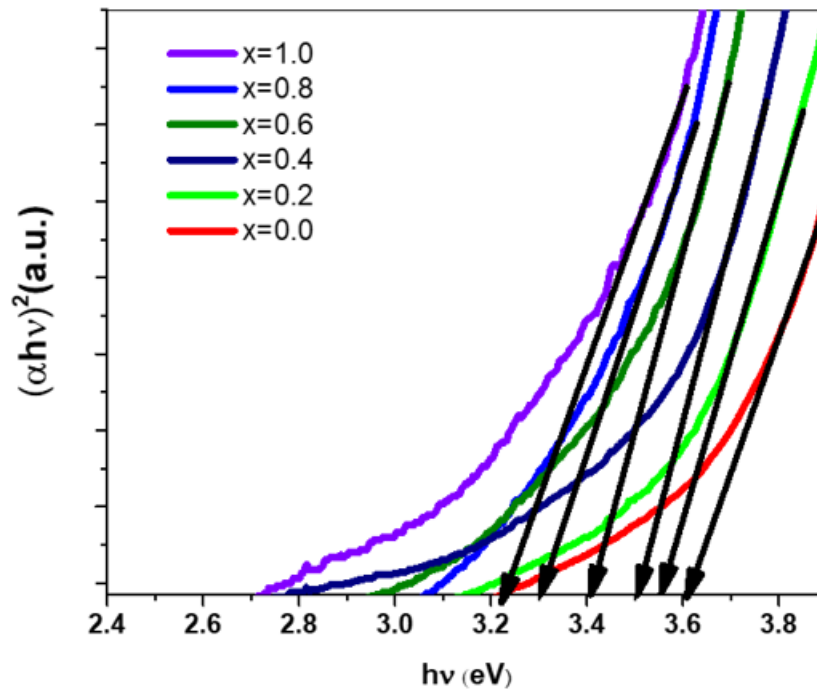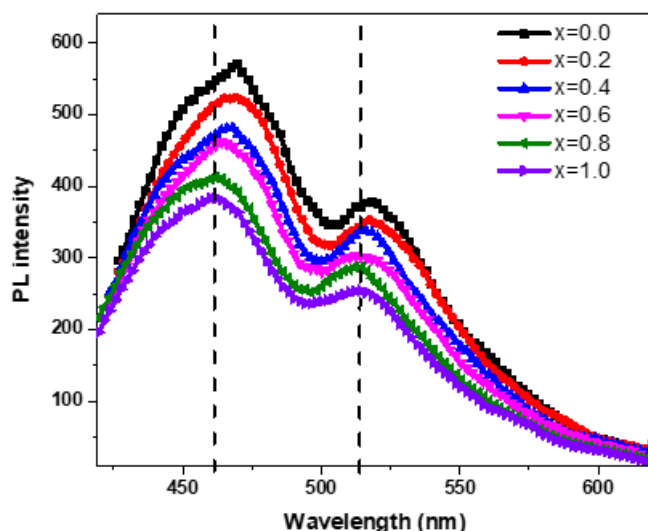

Figure 8: Energy gap spectra of $Cu_{1-x}Mn_xFe_2O_4$
(x = 0.0, 0.2, 0.4, 0.6, 0.8 and 1.0) nanoferrite.

When manganese ions are added to $CuFe_2O_4$ ferrites, a number of variables including impurities, carrier concentrations, crystallite size, and lattice strain, lead to a rise in the optical band gap. Moreover, creating defects, which causes the reduction in band gaps, is directly caused by the occurrence of higher oxidation levels of manganese in all circumstances [59].

3.5 Photoluminescence (PL) Studies

For studying the luminescence characteristics and recombination processes of semiconductor materials, photoluminescence (PL) spectroscopy is used, which provides information regarding the sub-band gap nanostructures of $CuFe_2O_4$. All samples showed a luminescence peak in the observable range from 420 and 600 nm, indicating that there are defects and oxygen vacancies [60]. $Cu_{1-x}Mn_xFe_2O_4$ (x = 0.0, 0. 2, 0. 4, 0. 6, 0. 8, 1.0) sample PL spectra were captured in **Figure** 9 at ambient temperature, with the stimulation recorded at a wavelength of 400 nm.

Figure 9: Photoluminescence spectra of $Cu_{1-x}Mn_xFe_2O_4$
(x = 0.0, 0.2, 0.4, 0.6, 0.8 and 1.0) nanoferrite.

In the current investigation, pure $CuFe_2O_4$ and copper ferrites doped with Mn both displayed two peaks, at 461, 463, 464, 465, 467, and 469 nm showing the blue emissions, while at 512, 513, 515, 516, 518, and 519 nm shows the green emissions. Blue emission is shown in the first peak that results from radiative flaws caused by the interface traps at the grain boundaries. [61,62]. The oxygen vacancies are responsible for the second peak [63]. While the single-ionized oxygen vacancy and trap-state emission are the usual titles for the green emission peak [64]. New electronic levels lying between the conductive band and the valence band, may have arisen due to an increase in intrinsic defects, which is what causes this behavior to occur. As a result, the processes, which are impacted by flaws, control the emission properties of copper ferrites. Also, it was discovered that Mn doping in copper ferrite matrix enhances the x values, which strengthens the luminescence. Even though samples' defects control the processes, the luminescence intensity increases according to the growing distance between the dopant which is considered as an activator and the array [65]. The Cu_{1-}

$_xMn_xFe_2O_4$ ferrites' disorder centers function as trap levels, whereas Mn^{2+} activators increase the luminescence's intensity, and Vijaya et al. showed similar results in earlier publications [48]. $CuFe_2O_4$ will have larger particles after the addition of Mn^{2+}, which is shown in the red shift in the Photoluminescence spectra.

3.6 Magnetic Measurements

The characteristics of spinel ferrites have an acknowledgeable impact on the magnetic interactions in the tetrahedral and octahedral sites as well as on the cation-distribution in these sites [66]. The change in Mn/Cu concentration ratio leads to a shift in cation distribution and exchange connections, which changes the magnetic properties. Two sub-lattices make up the ideal spinel structure, where the tetrahedral (A) and octahedral (B) sites have different metal cation charge distributions. Therefore, the vast majority of the magnetic characteristics of spinel ferrite are governed by the metallic ions type and the cations distribution between sites A and B.
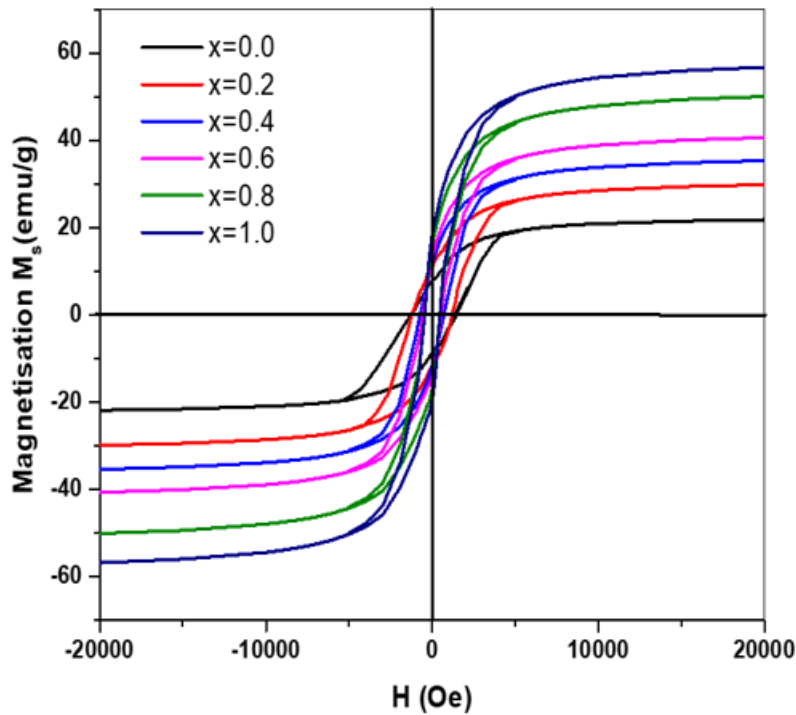
Figure 10: Magnetic hysteresis loops of $Cu_{1-x}Mn_xFe_2O_4$ (x = 0.0, 0.2, 0.4, 0.8 and 1.0) system.

Magnetic studies of each sample reveal a soft and ferromagnetic nature [67–69]. The current research shows that the magnetic characteristics of $Cu_{1-x}Mn_xFe_2O_4$ (x= 0.2, 0.4, 0.6, 0.8, and 1.0) were evaluated through SQUID with the greatest magnetisation of +4,376.76 kA/m (+55 kOe) at ambient temperature. **Figure** 10 displays the magnetic hysteresis loops for each sample

Table 2 lists the various variables, including saturation magnetisation (Ms), remnant (Mr), coercivity (Hc), (Mr/Ms), and magnetic moment (B).

X	Saturation magnetisation M_s (emu/g)	Remanent magnetisation M_r (emu/g)	Coercivity H_c (Oe)	M_r/M_s	Magnetic moment ηB (μ_B)
0	49.1	20.3	1400	0.41	2.1
0.2	54.7	21	1234	0.38	2.3
0.4	58.5	21.3	770	0.36	2.51
0.6	65.45	22.1	730	0.34	2.8
0.8	70.2	22.5	555	0.32	3.007
1.0	73.2	24.5	460	0.334	3.14

Table 2: The values of $Cu_{1-x}Mn_xFe_2O_4$ nanoparticles' magnetic properties, Ms, Mr, Hc, Mr/Ms, and B, at x=0, 0.2, 0.4, 0.8, and 1.0 and 1.0
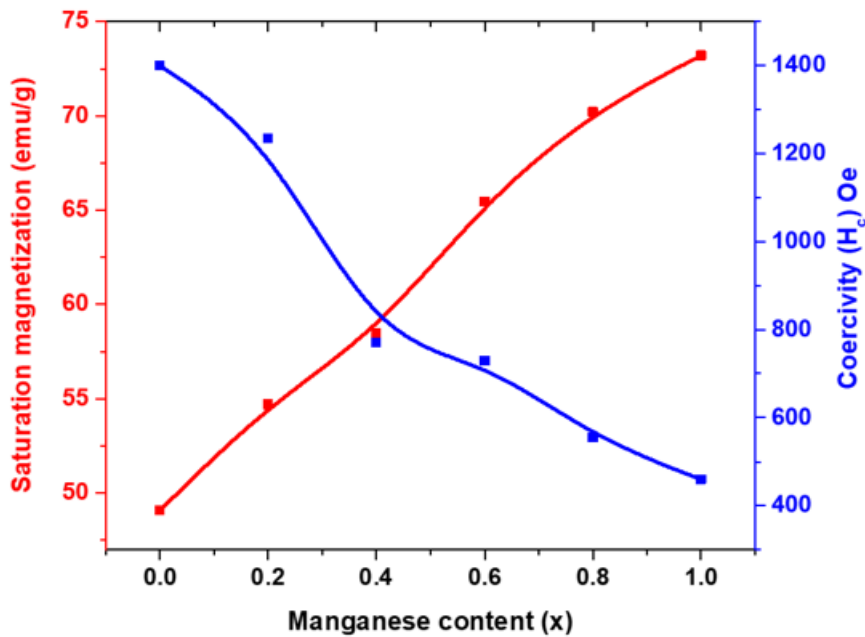
**Figure 11: Coercivity Hc and saturation magnetization Ms of Cu$_{1-x}$Mn$_x$Fe$_2$O$_4$
as a function of copper percentage x.**

Ms and Mr have been observed to increase when copper substitution does. As shown in **Figure** 11 and **Table** 2, the Ms rises from 35.5 to 73.2 emu g-1 as x rises from 0 to 1.0. Bulk MnFe$_2$O$_4$ has a Ms value of 110.6 emu/g [70].

In this instance, utilising a TEA-assisted route procedure, pure MnFe$_2$O$_4$ nanoparticles with diameters of 20 nm were found to have Ms values of 73.2 emu/g, which are greater than the values of 67 emu/g for MnFe$_2$O$_4$ crystallites with 1 m diameters [71]. The difference that has been noticed might be a result of something like size, shape, crystallinity, magnetisation orientation, etc. The potential substitution of Mn^{2+} for Cu^{2+} at the tetrahedral positions of the spinel ferrite lattice helps to explain the increase in Ms with Mn^{2+} presence.

These outcomes in the Ms version can be explained by Neel's dual sub-lattice magnetisation model [72, 73, 36]. This magnetisation-based model is built on the equation M (in B) = MB - MA, wherein MA and MB are the net magnetic moments of the tetrahedral and octahedral sites, respectively. Based on Neel scheme, the Ms values are raised by raising the proportion of B sites with magnetic Fe^{3+} or Mn^{2+} ions [48]. Where the Ms values grow as the Mn^{2+} level as a result of the increased utilisation of Fe^{3+} and Mn^{2+} at B sites.

Also, the saturation magnetisation improvement results from the greater magnetic moment of Mn^{2+} (5 μB) in contrast to the replacement equivalent Cu^{2+} (1 μB). As a result, the magnetic moment of the Mn^{2+} ion doping samples rose overall as the manganese doping increased, subsequently increasing the magnetic moment in the B-sub lattice. Recently, doped copper ferrite found similar outcomes [72]. The data shown in **Table** 2 clearly show that the coercivity

(H$_c$) for the samples of CuFe$_2$O$_4$ and MnFe$_2$O$_4$ drastically dropped from 1344 to 760 O$_e$, respectively (**Figure** 11).

A decreased anisotropy field, which reduces the energy of the domain wall, may be the cause of the fall in coercivity that is accompanied by an increase in manganese content. This, in turn, explains why cobalt ferrite exhibits excessive magneto-crystalline anisotropy, as the formula Hc = 2K/μoM shows the link between the coercivity and anisotropy constant [74]. As a result, Cu$_{1-x}$Mn$_x$Fe$_2$O$_4$ nanoferrites have a higher anisotropy constant due to the excessive magnetic anisotropy of Mn^{2+} ions [75].The coercivity tend to rise as the Mn^{2+} doping levels rises as stated by Vijaya et al. [48]. Oliveira et al. [76] disagreed with Vijaya's work, which supported our current observation. Consequently, it can be concluded that there are certain connections between the structural performance of the Cu$_{1-x}$Mn$_x$Fe$_2$O$_4$ system and its magnetic properties. The lattice parameter increased to 8.371 Å due to Mn doping leading to expanding the unit cell volume and lengthening the space between the atoms of the divalent and trivalent ions, all of which had an impact on the magnetic characteristics. The magnetic moment can be obtained through the following relationship and is shown in **Table** 2 as Bohr magneton units (μB) of the experimental value [77].

$$\eta_B = \frac{M \times M_s}{5585} \qquad (4)$$

Where "M" stands for molecular weight and "Ms" for saturation magnetisation.

The strength of the super-exchange interactions among the numerous sites increased the values, and caused them to rise. In our example, **μ_B** was discovered to rise when Mn^{2+} levels rose (see **Figure** 12). Magnetron number μ_B measured values are shown in **Table** 2. As x increases, the pattern of μ_B values increases, which may be related to x increasing in MS. Additionally, the ratio of Mr to Ms (Mr/Ms) declined as the Mn concentration rose. Table 2 shows the Mr/Ms values for $Cu_{1-x}Mn_xFe_2O_4$ ferrites, which range from 0.57 to 0.47.
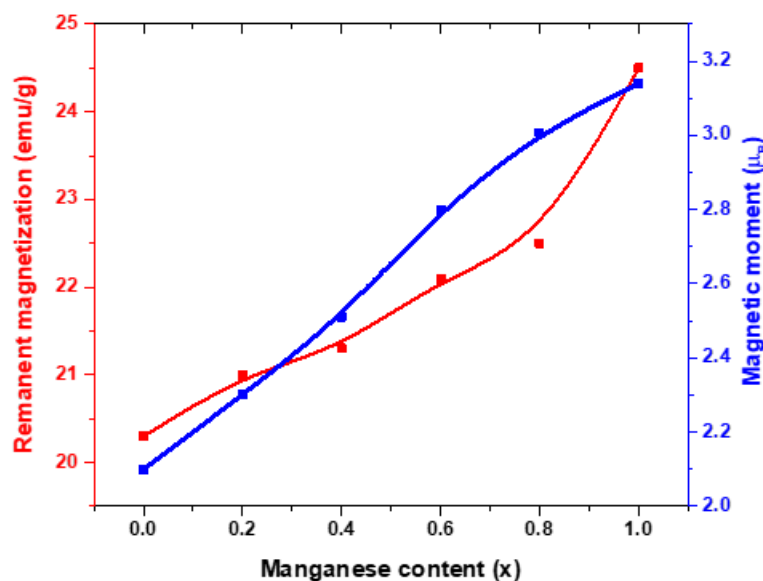
Fig. 12. Variations of Mr and µB versus copper content x in Cu1-xMnxFe2O4.

These values are less than the "1.0" value that is predicted for single domain ferromagnetic samples. Detected deviation from unity (1) could result from interactions between the grains, which may be caused by the material's distribution of particle sizes [78,79]. The acquired magnetic measurements in this work demonstrate the ferromagnetic nature of $Cu_{1-x}Mn_xFe_2O_4$ nanoferrites. As a result, they are great options for a variety of applications; microwave and biomedicine among them.

4. CONCLUSION

Co-precipitation was used to create Cu1-xMnxFe2O4 nanoferrites, which were then used to study how manganese substitution affected the structural, optical, and magnetic properties of copper ferrites. The optical, grain size, and magnetic properties are significantly impacted by manganese substitution variability. However, the lattice constant rises from 8.452 to 8,472 because the ionic radius of Mn2+ is greater than that of Cu2+. The nanoparticles' size changed from 10.2 to 25 nm with increasing Mn content. The band gap energy of nanoferrites reduces from 3.61 eV to 3.23 eV as Mn2+ ion concentration rises. In copper ferrite matrices, it has been found that the luminescence intensity rises as the Mn2+ ratio rises. Additionally, when Mn2+ replaces Cu2+, saturation magnetisation, and remanent magnetisation decline. All of the prepared nanoferites were found to be ferromagnetic according to the SQUID tests, and the Ms values for pure samples were 20.3 emu/g and 72.45 emu/g for MnFe2O4, respectively. The findings of the research are presented for further investigation.

REFERENCES

1. Rodrigues, A.R.O.; Ramos, J. M. F.; Gomez, I. T.; Almeida, B. G.; Araújo, J. P.; Queiroz, M. J. R. P.; Coutinho, P. J. G.; Castanheira, E. M. S., *RSC Adv.*, 2016, *6*, 17302-17313.
2. Gupta, A.K.; Naregalkar, R. R.; Vaidya, V. D.; Gupta, M., *Nanomedicine*, 2007, *2*, 23-39.
3. Mohseni, H.; Shokrollahi, H.; Sharifi, I.; Gheisari, Kh., *J. Magn. Magn. Mater.*, 2012, *324*, 3741-3747.
4. Somvanshi, S. B.; Kharat, P. B.; Khedkar, M. V.; Jadhav, K.M., *Ceram. Int.*, 2020, *46*, 7642-765.
5. Mohapatra, J.; Mitra, A.; Bahadur, D. ; Aslam M. M., *CrystEngComm*, 2013, *15*, 524-532.
6. Patade, S. R.; Andhare, D. D.; Somvanshi, S. B.; Kharat, P. B.; More, S. D.; Jadhav, K.M., *Nanomater. Energy,* 2020, *9*, 8-13.
7. Kale, S. B.; Somvanshi, S. B.; Sarnaik, M. N.; More, S. D.; Shukla, S. J.; Jadhav, K.M., *2nd International Conference on Condensed Matter and Applied Physics*, Bikaner, AIP Publishing, Long Island, 2018.
8. Somvanshi, S.B.; Kumar, R. V.; Kounsalye, J. S.; Saraf T. S.; Jadhav, K.M., *Proceedings of DAE Solid State Physics Symposium*, Hisar, AIP Publishing, Long Island, 2019.

9. Somvanshi, S.B.; Khedkar, M. V.; Kharat, P. B. ; Jadhav, K.M., *Ceram. Int.*, 2020, *46*, 8640-8650.

10. Bharati, V.; Somvanshi, S.B.; Humbe, A. V.; Murumkar, V.D.; Sondur, V.V. ; Jadhav, K.M., *J. Alloys Comp.*, 2020, *821*, 153501.

11. Manikandan, A.; Vijaya, J. J.; Kennedy L. J., *Physica E: Low-dimntional Systems and Nanostructures*, 2013, *49*, 117–123.

12. Maruthamani, D.; Vadivel, S.; Kumaravel, M.; Saravanakumar, B.; Bappi, P.; Dhar, S. S.; Habibi-Yangjeh, A.; Manikandan A.; Ramadoss, G., *J. Colloid Interface Sci.*, 2017, *498*, 449-459.

13. Asiri, S.; Sertkol, M.; Guner, S.; Gungunes, H.; Batoo, K. M.; Saleh, T. A.; Sozeri, H.; Almessiere, M. A.; Manikandan, A.; Baykal, A., *Ceram. Int.*, 2018, *44*, 5751–5759.

14. Mathubala, G.; Manikandan, A.; Arul Antony, S.; Ramar, P., *Nanosci. Nanotechnol. Lett.*, 2016, *8*, 375–381.

15. Deraz, NM. ; Alarifi, A., *Journal of Analytical and Applied Pyrolysis,* 2012, *94*, 41-47.

16. Silambarasu, A.; Manikandan, A.; Balakrishman, K., *J. Supercond. Novel Magn.*, 2017, *30*, 2631–2640.

17. Ravichandran, A. T.; Srinivas, J.; Karthick, R.; Manikandan, A.; Baykal, A., *Ceram. Int.*, 2018, *44*, 13247–13252.

18. Rajmohan, S.; Rani, J.; Manikandan, A.; Pragasam, J., *Nanosci. Nanotechnol. Lett.*, 2016, *8*, 393–398.

19. Rajendiran, A.; Jeyadevan, B.; Vaidyanathan, G.; Sendhilnathan, S., *J. Magn. Magn. Mater.*, 2005, *288*, 470–477.

20. Fujioka, H.; Ikeda, T.; Ono, K.; Ito, S.; Oshima, M., *J. Cryst. Growth*, 2002, *241*, 309–312.

21. Salah, L. M.; Moustafa, A. M.; Ahmed Farag, I. S., *Ceram. Int.*, 2012, *38*, 5605–5611.

22. Zuo, X.; Yang, A.; Vittoria, C.; Harris, V.G., *Journal of Applied Physics,* 2006, *99*, 08M909.

23. Yao, C.; Zeng, Q.; Goya, G.F.; Torres, T.; Liu, J.; Wu, H.; Ge, M.; Zeng, Y.; Wang, Y.; Jiang, J.Z., *J. Phys. Chem. C,* 2007, *111*, 12274-12278.

24. Xuan, Y.; Li, Q.; Yang, G., *J. Magn. Magn. Mater.*, 2007, *312*, 464-469.

25. Wang, W.; Zang, C.; Jiao, Q., *J. Magn. Magn. Mater.*, 2013, *349*, 116-120.

26. Isfahani, M. J. N.; Myndyk, M.; Menzel, D.; Feldhoff, A.; Amighian, J. ; Sepelak, V., *J. Magn. Magn. Mater.*, 2009, *321*, 152-156.

27. Mohseni, H.; Shokrollahi, H.; Sharifi, I.; Gheisari, Kh., *J. Magn. Magn. Mater.*, 2012, *324*, 3741-3747.

28. Isfahani, M. J. N.; Myndyk, M.; Sepelak, V.; Amighian, J., *J. Alloys Comp.,* 2009, *470*, 434-437.

29. Hessien, M. M.; Rashad, M. M.; El-Barawy, K.; Ibrahim, I. A., *J. Magn. Magn. Mater.,* 2008, *320*, 1615- 1621.

30. Patade, S. R.; Andhare, D. D.; Somvanshi, S. B.; Kharat, P. B.; More, S. D.; Jadhav, K.M., *Nanomater. Energy*, 2020, *9*, 1-7.

31. Balavijayalakshmi, J.; Suriyanarayanan, N.; Jayaprakash, R.; Gopalakrishnan, V., *Phys. Procedia*, 2013, *49*, 49–57.

32. Hashim, M.; Alimuddin; Kumar, S.; Koo, B. H.; Shirsath, S. E.; Mohammed, E. M.; Shah, J.; Kotnala, R. K.; Choi, H. K.; Chung, H.; Kumar, R., *J. Alloys Comp.*, 2012, *518*, 11–18.

33. Sanpo, N.; Wang, J.; Berndt, C. C., *J. Nano Res.*, 2013, *22*, 95–106.

34. Balavijayalakshmi, J.; Suriyanarayanan, N.; Jayapraksah, R., *Mater. Lett.*, 2012, *81*, 52–54.

35. Bammannavar, B. K.; Naik, L. R.; Pujar, R. B.; Chougule, B., *Prog. Electromagn. Res. Lett.*, 2008, *4*, 121–129.

36. Singh, C.; Bansal, S.; Kumar, V.; Tikoo, K. B.; Singhal, S., *RSC Adv.*, 2015, *5*, 39052–39061.

37. Azam, A., *J. Alloys Comp.*, 2012, *540*, 145–153.

38. Jnaneshwara, D. M.; Avadhani, D. N.; Prasad, B. D.; Nagabhushana, H.; Nagabhushana, B. M.; Sharma, S. C.; Prashantha, S. C.; Shivakumara, C., *Spectrochimica Acta Part A: Molcular and Biomolecular Spectroscopy*, 2014, *132*, 256–262.

39. Villette, C.; Tailhades, P.; Rousset, A., *J. Solid State Chem*, 1995, *117*, 64–72.

40. Lontio, R.; Kenfack, P.; Magnin, D.; Hermans, S.; Delcorte, A.; Lambi, J., *J. Solid State Chem.*, 2015, *230*, 381–389.

41. Hankare, P.P.; Kamble, P.D.; Kadam, M.R.; Rane, K.S.; Vasambekar, P.N., *Mater. Lett.*, 2007, *61*, 2769–2771.

42. Tanaka, Y.; Maenosono, S., *J. Magn. Magn. Mater.*, 2008, *320*, L121- L124.

43. Gautam, S.; Muthurani, S.; Balaji, M.; Thakur, P.; Padiyan, D. P.; Chae, K.; Kim, S.; Asokan, K., *J. Nanosci. Nanotechnol.*, 2011, *11*, 386-390.

44. Tailhades, Ph.; Villette, C.; Rousset, A.; Kulkarni, G.U.; Kannan, K.R., *Journal of Solid State Chemistry*, 1998, *141*, 56–63.

45. Rath, C.; Anand, S.; Das, R.P.; Sahu, K.K.; Kulkarni, S.; Date, S.; Mishra, N.C., *Journal of Applied Physics*, 2002, *91*, 2211-2215.

46. Azab, A.; El-Khawas, E. H., *Journal of Applied Sciences Research*, 2013, *9*, 1683-1689.

47. Salah, L. M.; Moustafa, A. M.; Ahmed Farag, I. S., *Ceram. Int.*, 2012, *38*, 5605–5611.

48. Vijaya, J. J.; Sekaran, G.; Bououdin, M., *Ceram. Int.*, 2015, *41*, 15–26.

49. Kumar, E. R.; Jayaprakash, R.; Devi, G. S.; Reddy, P. S. P., *J. Magn. Magn. Mater.*, 2014, *355*, 87–92.

50. Hammad, T. M.; Salem, J.K.; Abu Amsha, A.; Hejazy, N.K., *J. Alloys Comp.*, 2018, *741*, 123-130.

51. Tanaka, Y.; Maenosono, S., *J. Magn. Magn. Mater.*, 2008, *320*, L121.

52. Pankhurst, Q. A.; Connolly, J.; Jones, S. K.; Dobson, J. J., *Journal of Physics D: Applied Physics*, 2003, *36*, R167.

53. Gautam, S.; Muthurani, S.; Balaji, M.; Thakur, P.; Padiyan, D. P.; Chae, K.; Kim, S.; Asokan, K., *J. Nanosci. Nanotechnol.*, 2011, *11*, 386-390.

54. Rana, M. U.; Misbah-ul-Islam; Abbas, T., *Mater. Lett.*, 1999, *41*, 52-56.

55. Hammad, T. M.; Salem, J. K.; Harrison, R. G., *Superlattices Microstruct.*, 2010, *47*, 335-340.

56. Rahman, S.; Nadeem, K.; Rehman, M.A.; Mumtaz, M.; Naeem, S.; Papst, I.L., *Ceram. Int.*, 2013, *39*, 5235–5239.

57. Hammad, T. M.; Salem, J. K.; Abu Shanab, N.; Kuhn, S.; Hempelmann, R., *J. Lumin.*, 2015, *157*, 88–92.

58. Joseph, D.P.; Venkateswaran, C., *J. At., Mol., Opt. Phys.*, 2011, *2011*, 270450.

59. Sharma, S.; Ramesh, P.; Swaminathan, P., *Journal of Electronic Matererials*, 2015, *44*, 4710-4716.

60. Freedsman, J. J.; Kennedy, L. J.; Kumar, R.T.; Sekaran, G.; Vijaya, J. J., *Mater. Res. Bull.*, 2010, *45*, 1481–1486.

61. Zang, C. H.; Zang, D. M.; Tang, C. J.; Fang, S. J.; Zong, Z. J.; Yang, Y. X.; Zhao, C. H.; Zhang, Y. S., *J. Phys. Chem. C*, 2009, *113*, 18527.

62. Zhuge, L. J.; Wu, X. M.; Wu, Z. F.; Yang, X. M.; Chen, X. M.; Chen, Q., *Journal of Materials Chemistry and Physics*, 2010, *120*, 480-483.

63. Bhargava, R.; Sharma, P. K.; Dutta, R. K.; Kumar, S.; Pandey, A. C.; Kumar, N., *Journal of Materials Chemistry and Physics*, 2010, *120*, 393-398.

64. Costa, A. C. F. M.; Kiminami, R. H. G. A.; Santos, P. T. A.; Silva, J. F., *J. Mater. Sci.*, 2013, *48*, 172.

65. Anh, L. N.; Loan, T. T.; Duong, N. P.; Soontaranon, S.; Viet Nga, T. T.; Hien, T. D., *J. Alloys Comp.*, 2015, *647*, 419-426.

66. Phumying, S.; Labuayai, S.; Swatsitang, E.; Amornkitbamrung, V.; Maensiri, S., *Mater. Res. Bull.*, 2013, *48*, 2060–2065.

67. Lin, X.; Lv, X.; Wang, L.; Zhang, F.; Duan, L., *Mater. Res. Bull.*, 2013, *48*, 2511–2516.

68. Guo, P.; Zhang, G.; Yu, J.; Li, H.; Zhao, X. S., *Colloids and Surfaces A: Physicochemical and Engineering Aspects*, 2012, *395*, 168–174.

69. Ahmad, I.; Abbas, T.; Islam, M. U.; Maqsood, A., *Ceram. Int.*, 2013, *39*, 6735–6741.

70. Balaji, G.; Gajbhiye, N. S.; Wilde, G.; Weissmuller, J., *J. Magn. Magn. Mater.*, 2002, *242–245*, 617–620.

71. Zhang, D.; Zhang, X.; Ni, X.; Song, J. M.; Zheng, H., *Chem. Phys. Lett.*, 2006, *426*, 120–123.

72. Bhasker, S. U.; Reddy, M. V. R., *J. Sol-Gel Sci. Technol.*, 2015, *73*, 396–402.

73. Bhukal, S.; Namgyal, T.; Mor, S.; Bansal, S.; Singhal, S., *J. Mol. Struct.*, 2012, *1012*, 162–167.

74. Baldi, G.; Bonacchi, D.; Innocenti, C.; Lorenzi, G.; Sangregorio, C., *J. Magn. Magn. Mater.*, 2007, *311*, 10–16.

75. Ammar, S.; Helfen, A.; Jouini, N.; Fi´evet, F.; Rosenman, I.; Villain, F.; Molinie, P.; Danot, M., *Journal of Meterials Chemistry*, 2001, *11*, 86-192.

76. Oliveira, V. D.; Rubinger, R. M.; Silva, M. R.; Oliveira, A. F.; Rodrigues, G., *Materials Research*, 2016, *19*, 786-790.

77. Moradmard, H.; Shayesteh, S. F.; Tohidi, P.; Abbas, Z.; Khaleghi, M., *J. Alloys Comp.*, 2015, *650*, 116–122.

78. Gopalan, E. V.; Joy, P. A.; Al-omari, I. A.; Kumar, D. S.; Yoshida, Y.; Anantharaman, M. R., *J. Alloys Comp.*, 2009, *485*, 711–717.

79. Ayyappan, S.; Mahadevan, S.; Chandramohan, P.; Srinivasan, M. P.; Philip, J.; Raj, B., *J. Phys. Chem. C*, 2010, *114*, 6334–6341.